Model-independent predictions for smooth cosmic acceleration scenarios

V. Miranda[1] and Cora Dvorkin[2]

[1]Center for Particle Cosmology, Department of Physics and Astronomy, University of Pennsylvania, Philadelphia, Pennsylvania 19104, USA

[2]Harvard University, Department of Physics, Cambridge, Massachusetts 02138, USA

(Received 9 January 2018; published 30 August 2018)

Through likelihood analyses of both current and future data that constrain both the expansion history of the Universe and the clustering of matter fluctuations, we provide falsifiable predictions for three broad classes of models that explain the accelerated expansions of the Universe: ΛCDM, the quintessence scenario, and a more general class of smooth dark energy models that can cross the phantom barrier $w(z) = -1$. Our predictions are model independent in the sense that we do not rely on a specific parametrization, but we instead use a principal component (PC) basis function constructed *a priori* from a noise model of supernovae and cosmic microwave background observations. For the supernovae measurements, we consider two type of surveys: the current JLA and the upcoming WFIRST surveys. We show that WFIRST will be able to improve growth predictions in curved models significantly. The remaining degeneracy between spatial curvature and $w(z)$ could be overcome with improved measurements of $\sigma_8\Omega_m^{1/2}$, a combination that controls the amplitude of the growth of structure. We also point out that a PC-based figure of merit reveals that the usual two-parameter description of $w(z)$ does not exhaust the information that can be extracted from current data (JLA) or future data (WFIRST).

DOI: 10.1103/PhysRevD.98.043537

I. INTRODUCTION

The source of the current accelerated expansion of the Universe, discovered almost two decades ago [1,2], remains one of the most intriguing puzzles of our time. From an exotic component with negative pressure to a break of general relativity on cosmological scales, many explanations have been theorized. Moreover, large experimental efforts [3–16] either have been made, are in progress, or are currently being proposed to measure the expansion history of the Universe and growth of structure with percent-level precision (or better).

Various parametrizations of the dark energy equation of state have been thoroughly studied in the literature [17–28]. In this work, we study a broader class of cosmic acceleration scenarios, modeling the equation of state $w(z)$ by a principal component (PC) basis function, following previous works [29–31]. We analyze a broad class of scenarios with a constant or time-dependent (but smooth) equation of state, with and without spatial curvature. This work provides both an update of the current state of the art on constraints on the Hubble expansion rate, as a function of redshift, the luminosity distance, and the growth of structure, and predictions for the upcoming surveys. We use the constraints from current and future measurements to make predictions for other cosmic acceleration observables. Specifically, we use both current measurements of supernovae (JLA) and future measurements (WFIRST), observations of the cosmic microwave background (CMB) temperature and polarization power spectra by the Planck satellite, baryon acoustic oscillations, and the Hubble constant. The results of this work can be used as a ground test for dark energy scenarios, a violation of which could potentially rule out a whole class of acceleration paradigms.

We will divide our cosmological observables into those providing us information about the geometry of the Universe and those with information about the clustering of matter. In the context of smooth dark energy models, dark energy affects the growth of structures only through the background expansion. This assumption enables a consistency check by comparing observables that are sensitive to the background expansion and to the growth of linear perturbations, which is violated only in models that either modify general relativity or predict the clustering of the dark energy itself. Therefore, the rate of evolution of the growth functions with redshift is a powerful probe of dark energy [32,33]. However, one should be cautious when interpreting consistency tests based on particular parametrizations because growth and geometry probes are sensitive to the evolution of the dark energy equation of state in different ways, and therefore wrong assumptions on the redshift behavior of $w(z)$ could induce misleading discrepancies. On the other hand, the choice of a particular parametrization has the advantage of being more computationally efficient, and can falsify interesting scenarios such as $w(z) =$ constant. This paper offers a complementary

TABLE I. Data sets that define the Geo, All, and All w/o WL-RSD group of chains.

	(a) Geo	(b) All	(c) All w/o WL-RSD
CMB	Gaussian	Full Planck (including lensing reconstruction)	Full Planck
BAO	DR12 + WiggleZ + 6DF + MGS	DR12 (including RSD) + WiggleZ + 6DF + MGS	DR12 + WiggleZ + 6DF + MGS
H_0	Riess *et al.* 2016	Riess *et al.* 2016	Riess *et al.* 2016
SN	JLA or WFIRST	JLA	JLA
WL	...	CFHTLens (including nonlinear scales)	...

approach to previous efforts [32,33] that relied on specific functional forms for $w(z)$.

Another appealing possibility is to use $w(z)$ PCA to examine in detail how systematic effects and different survey strategies induce changes in the dark energy equation of state [34]. In the context of WFIRST, Ref. [5] provides a detailed analysis on the relative importance of various systematic uncertainties, as well as the differences in the figure of merit between a space survey that carries an onboard integral field channel (IFC) spectrometer and a strategy that assumes that spectra will be observed from the ground. It would be interesting to understand how much their conclusions depend on the parametrization adopted, which we postpone for future work to be accomplished in collaboration with the WFIRST supernova science investigation teams.

This paper is organized as follows. In Sec. II we discuss the data and broad classes of models that we use in our analysis. In Sec. III we present our main results, where we analyze the falsifiability of smooth dark energy scenarios [ΛCDM, quintessence, and more general smooth dark energy models that cross the phantom barrier of $w(z) = -1$] in a model-independent way. In Sec. IV we discuss the model-independent definition of the figure of merit, first proposed in Ref. [35]. We then quantify, in Sec. V, the effects of marginalizing over spatial curvature on the different classes of dark energy scenarios studied and vice versa (we see the effect on the curvature posteriors after marginalizing over the dark energy parameters). We present our conclusions in Sec. VI.

II. DATA AND MODELS

We ran multiple Markov chain Monte Carlo (MCMC) likelihood analyses with a modified version of the CosmoMC code [36–39]. Our chains were divided into three broad categories (see Table I): the first group, named Geo, contains data sets that probe only the geometry of our Universe. The second group, called All, also includes data sets that measure the linear and nonlinear evolution of the structure formation. The last group, named All w/o WL-RSD, is similar to Geo but we exchange the CMB compressed Gaussian likelihood [9][1] with the full CMB temperature and polarization power spectra measurements [40].

One of the aims of this paper is to assess how the posterior for spatial curvature depends on our assumptions about the behavior of $w(z)$. In this investigation, we introduce an additional data set—named All w/o WL-RSD—given that there is a well-known tension between CMB and weak lensing on the amplitude of perturbations that can bias such a posterior. The comparison between All w/o WL-RSD and All constraints indicates the magnitude of such biases.

In addition to these broad categories, our chains in the Geo group were further divided into two subgroups, depending on the adopted supernovae data set. The first subgroup uses the current JLA compilation implemented on CosmoMC [4], and the second one adopts WFIRST simulated data [5].

All the chains ran in this work included baryon acoustic oscillations (BAO) [41,42] and local H_0 measurements [43]. The local H_0 measurements are implemented in CosmoMC as a Gaussian prior in the inverse angular diameter distance at the effective redshift $z = 0.04$ [44]. Because the principal components allow $w(z)$ to vary in the redshift range $0 < z < 0.04$, PCAs introduce a dependency between the dark energy equation of state at low redshift and the predicted H_0 given a fixed inverse angular diameter distance, which broadens the H_0 posterior in comparison to ΛCDM.

Among all the different strategies presented in the WFIRST supernovae analysis [5], we adopted the so-called `Imaging-Allz`. That `Imaging-Allz` setup provides measurements of a few thousand type IA supernovae in a few redshift bins, observed over the broad redshift range $0 < z < 3$ (see Fig. 1). It does so by considering the scenario that a ground-based spectroscopy will be sufficient to calibrate the redshift evolution of the supernovae spectral features, which allows the WFIRST satellite to be solely an imaging survey. Complications of this hypothesis work in the direction of lowering the number of observed supernovae, increasing the systematic errors, and shortening the redshift range. We intend to address the impact that the different WFIRST strategies have in our conclusions in future work.

The All set of chains constrains the evolution of perturbations by adding the full lensed Planck temperature and polarization data [40], CMB lensing reconstruction [10], redshift space distortions [41], and tomographic CFHTLenS weak lensing data [46]. For both the CMB

[1]In the Geo chains, we have adopted the Gaussian compressed likelihood (not marginalized over the A_L parameter).

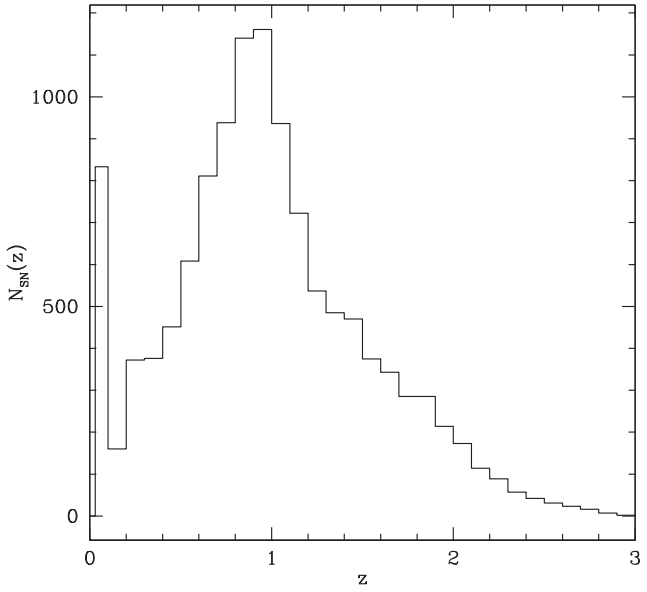

FIG. 1. Assumed type IA supernovae redshift distribution in the Imaging-Allz WFIRST strategy. The first bin ($0.01 < z < 0.1$) includes predictions for the number of type IA supernovae that will be observed by the Foundation supernovae survey [5,45].

lensing reconstruction and the CFHTLenS data sets, we have used range cuts that are less conservative than the ones adopted by the Planck Collaboration, as they include scales where gravitational collapse is nonlinear [9]. On the lensing reconstruction likelihood, we adopt the so-called aggressive cuts, and on the CFHTLenS weak lensing, we adopt the six bin tomographic likelihood. With the potential systematic contamination in mind, we do not overemphasize the statistical significance of deviations from ΛCDM.

To account for the nonlinear scales in the matter power spectrum, we adopt the HALOFIT fit [47]. Given that HALOFIT has only been calibrated to models with a constant dark energy equation of state, we apply the mapping described in Ref. [48] between a general time-evolving dark energy equation of state and $w = \text{const}$. This mapping has been tested against simulations for the well-known $w_0 - w_a$ dark energy parametrization, and we assume that the arguments presented in Refs. [48,49] that justify this mapping are also valid here. Indeed, the authors of Ref. [49] have argued that the nonlinear completion (of the power spectrum) of rapidly varying $w(z)$ models can be obtained from $w = \text{const}$ models by matching the distance to the last scattering surface.

We fix the sum of the neutrino masses as $\sum m_\nu = 0.06$ eV in all the chains. In a future paper, we will analyze how the sum of neutrino masses is affected when marginalizing over different assumptions on the dark energy equation of state.

In this paper we give an up-to-date status of the falsifiability of smooth dark energy models beyond ΛCDM. Furthermore, we analyze the impact of marginalizing different dark energy scenarios on parameters like the curvature on spatial slicings, Ω_K, and how measurements of a parameter that monitors local structure, $S_8 \equiv \Omega_m^{1/2}\sigma_8$, are relevant to constraining dark energy and Ω_K simultaneously.[2] Instead of performing a case-by-case analysis, we chose to do a model-independent analysis using a principal component basis, given that the main advantage of this basis is that it is complete.

We expand the dark energy equation of state as

$$w(z) = w_{\text{fiducial}} + \sum_{i=1}^{N_{\text{PC}}} \alpha_i e_i(z), \tag{1}$$

where $e_i(z)$ with $i = 1, \ldots, N_{\text{PC}}$ are the principal components of perturbation around the fiducial model $w_{\text{fiducial}} = -1$. These are shown in Fig. 2. The principal components have support in the range $0 < z < z_{\text{max}} = 3$. For $z > z_{\text{max}}$, we extrapolate the equation of state by assuming $w = w_\infty = \text{constant}$. Therefore, the energy density of dark energy is given by

$$\rho_{\text{DE}}(z) = \begin{cases} \rho_{\text{DE}}(0)\exp\left[3\int_0^z dz' \frac{1+w(z')}{1+z'}\right], & z \le z_{\text{max}} \\ \rho_{\text{DE}}(z_{\text{max}})\left(\frac{1+z}{1+z_{\text{max}}}\right)^{3(1+w_\infty)}, & z > z_{\text{max}}. \end{cases} \tag{2}$$

Here, and throughout this paper, we assume $w_\infty = -1$.

The parameter vector in the Geo chains is $\vec{\theta}_{\text{Geo}} = \{\Omega_c h^2, \theta_A, \alpha_1, \ldots, \alpha_{N_{\text{PC}}}, \Omega_K\}$. Here, $\Omega_c h^2$ is the cold dark matter density, θ_A is the angular size of the horizon at the time of recombination, H_0 is the local Hubble constant, and $h \equiv H_0/(100\ \text{km/s/Mpc})$. To reduce the dimensionality of the expensive MCMC chains, we fixed the baryon density $\Omega_b h^2 = 0.02228$ and the scalar tilt $n_s = 0.966$ in all the Geo chains, even though there is a correlation between these two quantities with the angular size of the CMB peaks and the so-called shift parameter $R = \sqrt{\Omega_m H_0^2} D_A(z_*)/c$ [9,50], where $D_A(z)$ is the comoving angular diameter distance to redshift z, and z_* is the redshift of recombination. Most of the constraining power on the amplitude of the principal components comes, however, from type IA supernovae and not from the CMB.

The baseline model for the chains in All and All w/o WL&RSD groups is

$$\vec{\theta}_{\text{All/Red}} = \vec{\theta}_{\text{Geo}} + \{\Omega_b h^2, n_s, \ln A_s, \tau\}. \tag{3}$$

Here, τ is the reionization optical depth; $\Omega_b h^2$ is the baryon density; and $\log A_s$ and n_s are the initial curvature power spectrum amplitude and tilt, respectively. The reionization history is assumed to be given by the so-called instantaneous reionization. Generalizations of the reionization

[2]The parameter σ_8 is defined as the rms amplitude in linear theory of mass fluctuations on an $8h^{-1}$ Mpc scale.

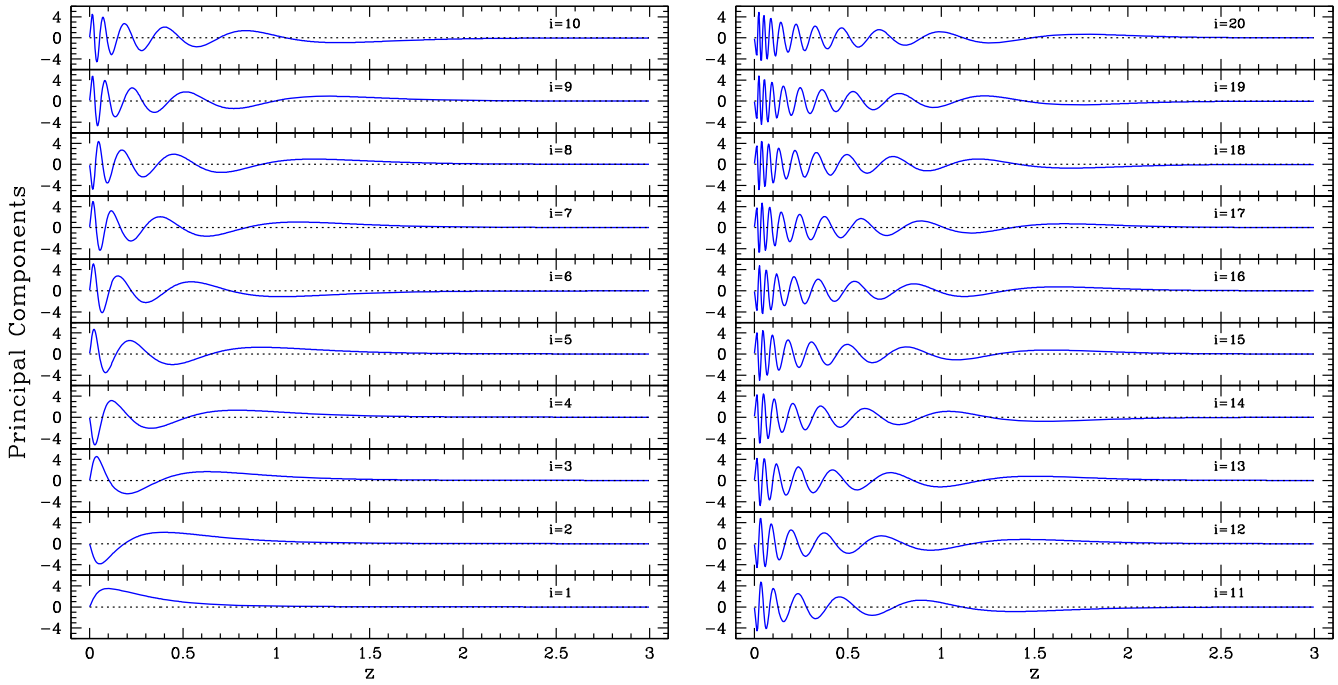

FIG. 2. The principal components of the dark energy equation of state, $w(z)$. The Fisher matrix used to construct this basis contains contributions from both type IA supernovae and the CMB. Lower components include fewer oscillations and have support, mainly, at low redshifts. Higher principal components oscillate rapidly at low redshifts, which suppresses their effect since there are two integrations in the scale factor to go from the equation of the state to the comoving luminosity distance. Their inclusion is, nevertheless, necessary to encompass the modes that supernovae can probe, with non-negligible statistical significance.

history that better fit the Planck LFI polarization data could potentially affect our results by changing the inferred $\ln A_s$, which then affects the gravitational lensing amplitude [51].

The growth function obeys the following evolution equation:

$$G'' + \left(4 + \frac{H'}{H}\right)G' + \left[3 + \frac{H'}{H} - \frac{3}{2}\Omega_m(z)\right]G = 0. \quad (4)$$

Here $H(z)$ is the Hubble function (we have neglected radiation), $\Omega_m(z) = \Omega_m(1+z)^3[H_0/H(z)]^3$, and prime denotes derivative with respect to $\ln a$. The normalization of the growth function at the initial redshift $z_{\rm ini} = 1000$ is $G(z_{\rm ini}) = 1$, and $G'(z_{\rm ini}) = -6\Omega_{\rm DE}(z_{\rm ini})/5$, where $\Omega_{\rm DE}(z) = [\rho_{\rm DE}(z)/\rho_{\rm DE}(0)][H_0/H(z)]^2$ [29]. Finally, the logarithm growth rate is defined as

$$f(z) \equiv \frac{d\ln D}{d\ln a} = 1 + \frac{G'}{G}. \quad (5)$$

Often, the parametrization $f(z) = \Omega_m(z)^\gamma$ is assumed [52], so we will also show how the so-called growth index γ varies as function of the redshift.

To construct the PC basis, we closely follow Appendix A of Ref. [29]. Here we will summarize the procedure and highlight the differences compared to Ref. [29]. We start with the supernovae Fisher matrix

$$\mathbf{F}^{\rm SN}_{ij} = \sum_\beta \sigma_\beta^{-2} \frac{dm(z_\beta)}{dp_i}\frac{dm(z_\beta)}{dp_j}, \quad (6)$$

where β runs through the redshift binning; m is the apparent magnitude $m(z) \equiv \mathcal{M} + 5\log(H_0 d_L(z))$; $\mathcal{M}$ is a constant related to the absolute magnitude; d_L is the luminosity distance; H_0 is the Hubble constant; $p_i = \{\beta_1, \ldots, \beta_{N_z}, \mathcal{M}, \Omega_m, \Omega_m h^2\}$; and $\{\beta_1, \ldots, \beta_{N_z}\}$ are the amplitudes of a binned dark energy equation of state. The eigenvectors of the Fisher matrix generate a basis for arbitrary functions defined on the redshift bins, $w(z_j) = w_{\rm fid} + \sum_{i=1}^{N_z} \alpha_i e_i(z_j)$. We construct piecewise-rectangular-shaped $w(z) = \beta_i$ if $z_{i-1} < z < z_i$ (and zero otherwise), which reduces the numerical noise in the final PCA shape because the energy density can be evaluated analytically.

The model for the statistical and systematic errors adopted in the supernovae Fisher matrix was updated relative to [29] to better represent the WFIRST Imaging-Allz simulated data:

$$\sigma_\beta^2 = \left(\frac{\Delta z}{\Delta z_{\rm sub}}\right)\left[\frac{s(z)}{N_\beta} + 0.01^2\left(\frac{1+z}{1.7}\right)^2\right], \quad (7)$$

with

$$s(z) = \begin{cases} 0.015 & z \le 1.03 \\ -0.014 + 0.014 \times (1+z) & z > 1.03. \end{cases} \quad (8)$$

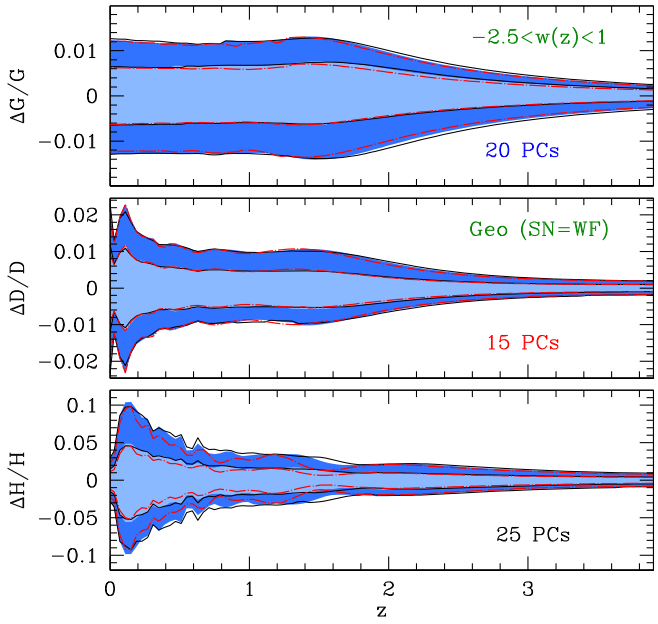

FIG. 3. Posterior for the growth function, the comoving luminosity distance, and the Hubble expansion rate (top to bottom) predicted by chains with 15 (dotted-dashed red lines), 20 (blue shaded areas), and 25 (solid black lines) principal components. The inner lines (and the darker blue shaded region) correspond to the width of the 68% confidence interval, while the outer lines (and the lighter blue shades) indicate the width of the 95% confidence area. All posteriors are centered at zero to guide the comparison of their width. In all three chains, we assumed flatness and the prior $-2.5 < w(z) < 1$. The likelihoods adopted in these chains are shown in Table I, with the supernovae data given by the simulated WFIRST data. The small differences in the Hubble posteriors are suppressed even further in the distance posteriors, which indicates that they reflect amplitude shifts in highly oscillatory modes. The small changes in distance and growth observables also confirm that 20 PCs are sufficient to ensure completeness of the PCA basis.

Here, N_β is the number of supernovae in each bin and $\Delta z = 0.1$, except for the first bin where $\Delta z = 0.1 - z_{\rm min}$ with $z_{\rm min} = 0.01$. We subdivided the data into $N_z = 883$ sub-bins up to $z_{\rm max} = 3$ (making $\Delta z_{\rm sub} = 0.003$), which corresponds to the maximum observable supernovae redshift in the WFIRST `Imaging-Allz` strategy [5]. The number of supernovae in the bins of $\Delta z = 0.1$ is shown in Fig. 1. As stated in Ref. [5], the systematic model adopted in our Fisher matrix is an oversimplification. More realistic likelihoods will, in practice, introduce correlations between the principal components. This, however, does not affect the conclusions of this paper since they do not depend on the orthogonality of the basis. The crucial point is that the PCA basis, although not orthogonal, is complete; i.e., it contains all the modes that can be observed by the WFIRST likelihood with high statistical significance. Indeed, Fig. 3 compares the posterior for the Hubble expansion rate, the growth function, and the comoving luminosity distance when 15, 20, and 25 principal components are varied. From here, it is clear that going from 15 to 25 PCs does not alter the observable posterior significantly.

To smooth the shape of the principal components, we apply the continuum limit; i.e., we increase the corresponding number of equal size bins to N_z, and then we impose the normalization

$$\sum_{i=1}^{N_z}[e_i(z_j)]^2 = \sum_{j=1}^{N_z}[e_i(z_j)]^2 = N_z. \tag{9}$$

We calculate the number of supernovae in each sub-bin via linear interpolation from the center of each original redshift bin. The factor $\Delta z/\Delta z_{\rm sub}$ rescales the errors in the sub-bins. Because the number of principal components ($N_{\rm PC}$) that ensures completeness with the data is much less than total number of bins, N_z, none of our results will depend on sub-bin width $\Delta z_{\rm sub}$. Last, we tested our procedure by explicitly reproducing the PCA basis shown in Ref. [29].

We also add a Planck-like likelihood to the total Fisher matrix. Similar to Ref. [29], we adopt the covariance matrix

$$\mathbf{C}^{\rm CMB} = \begin{bmatrix} (0.0018)^2 & -(0.0014)^2 \\ -(0.0014)^2 & (0.0011)^2 \end{bmatrix}, \tag{10}$$

for the parameters $\vec{q} = \{\ln(D_*/{\rm Mpc}), \Omega_m h^2\}$, where D_* is the comoving distance to the surface of the last scattering.[3] We then construct the CMB Fisher $\mathbf{F}^{\rm CMB} = \mathbf{D}[\mathbf{C}^{\rm CMB}]^{-1}\mathbf{D}^T$, where $\mathbf{D}_{ij} = dq_i/dp_j$.

Therefore, the total Fisher matrix is $\mathbf{F} = \mathbf{F}^{\rm SN} + \mathbf{F}^{\rm CMB}$. We then marginalize $\mathbf{F}$ over $\mathcal{M}$, Ω_m, and $\Omega_m h^2$. Supernovae measurements are insensitive to constant shifts in relative distances as well as shifts that are nearly constant at $z > z_{\rm min}$. As explained in Appendix B of Ref. [29], large variations in $w(z)$ below $z < z_{\rm min}$ create degeneracies between $\{\alpha_1, \ldots, \alpha_{N_{\rm PC}}\}$ and Ω_m that slow the convergence of the chains.

To ensure that the dark energy equation of state respects the prior $w_{\rm min} < w(z) < w_{\rm max}$, we follow the procedure described in Appendix A of Ref. [29]. We start from the projection of a generic $w(z)$ on the PC basis:

$$\alpha_i = \frac{1}{N_z}\sum_{j=1}^{N_z}[w(z_j) - w_{\rm fiducial}]e_i(z_j). \tag{11}$$

Now, the maximum/minimum α_i values are achieved whenever $w(z_j) = w_{\rm max}/w_{\rm min}$ and $e_i(z_j)$ is positive, and $w(z_j) = w_{\rm min}/w_{\rm max}$ and $e_i(z_j)$ is negative. Therefore, we require that $\alpha^{(-)} < \alpha < \alpha^{(+)}$, with

$$\alpha_i^{(\pm)} \equiv \frac{1}{N_z}\sum_{j=1}^{N_z}[(w_{\rm min} + w_{\rm max} - 2w_{\rm fiducial})e_i(z_j) \pm (w_{\rm max} - w_{\rm min})|e_i(z_j)|]. \tag{12}$$

[3]To evaluate D_*, we include radiation as well as cold dark matter and dark energy contributions.

Last, we further impose the prior on the sum

$$\sum_{i=1}^{N_z}[w(z_j)-w_{\rm fiducial}]^2 < \sum_{i=1}^{N_z}\max[(w_{\rm max}-w_{\rm fiducial})^2,(w_{\rm min}-w_{\rm fiducial})^2], \quad (13)$$

which implies

$$\sum_{i=1}^{N_{\rm PC}}\alpha_i^2 < \max[(w_{\rm max}-w_{\rm fiducial})^2,(w_{\rm min}-w_{\rm fiducial})^2]. \quad (14)$$

These are conservative priors because not all equations of state that respect the inequalities in Eqs. (12) and (14) are limited to the range $w_{\rm min} < w(z) < w_{\rm max}$, but the converse is true; i.e., the priors keep all the models we want and eliminate many models we need to exclude.

III. FALSIFYING SMOOTH DARK ENERGY

In this section, we investigate the falsifiability of smooth dark energy scenarios. The observables used here only constrain the background expansion of the Universe (Table I describes them in further detail). The data include local H_0 measurement, baryon acoustic oscillations, comoving distance to the surface of the last scattering, and type IA supernovae. They are collectively described as the Geo (SN = X) data sets, with $X =$ JLA or $X =$ WF (WFIRST) representing the adopted type IA supernovae data. In some aspects, this section provides a partial update to the analyses presented in Refs. [29,30]. The WFIRST supernovae data were simulated using state-of-the-art numerical tools, and the final likelihood takes into account a variety of systematic effects described in detail in Ref. [5].

Smooth dark energy models modify the amplitude of linear perturbations only through changes in the background evolution. Because the data contained in the Geo group are sensitive uniquely to the background expansion, the posteriors for the linear growth function are predictions that can be falsified with surveys that measure the amplitude of fluctuations. In fact, the Dark Energy Survey (DES) Collaboration already released its Year One data that can potentially falsify the predictions presented in this section. The WFIRST satellite, on the other hand, will release its supernovae results only by the end of the next decade and, at that time, it will also provide state-of-the-art weak lensing measurements that can be used to check the consistency between growth and geometry in smooth dark energy scenarios.

We examine chains that assume flatness, $\Omega_K = 0$, and others that allow spatial curvature to be a free parameter within some prespecified width. The prior of $-0.01 < \Omega_K < 0.01$ was adopted in chains with current type IA supernovae data, so predictions can be at the few-percent level. This prior is, indeed, informative except for ΛCDM models. Percent-level upper limits on $|\Omega_K|$ are at the order of what can be achieved by current data when growth information is included. For chains with simulated WFIRST type IA supernovae, the prior width is relaxed to $-0.1 < \Omega_K < 0.1$, which is not informative given the few-percent-level constraints we obtain in this case.

A. ΛCDM

In flat ΛCDM, the geometric data set with current JLA supernovae can constrain the comoving luminosity distance at the subpercent level at all redshifts, despite the fact that H_0 is measured at the 2.4% level. The Hubble expansion rate shows a striking tightness around $z \approx 0.9$, which was previously noted in Ref. [29]. With the CMB's outstanding precision in measuring the distance to the surface of last scattering, changes in the comoving distance at high redshift must be compensated by an opposite variation at low redshift where $D(z) \sim z/H_0$. Changes in H_0 at the few-percent level are, therefore, not compatible with the CMB and high-redshift type IA supernovae, even though they are allowed by local measurements. More precise local H_0 measurements would reduce uncertainties in predicting the comoving distance at high redshift in ΛCDM scenarios, which in turn would increase the ability of future type IA supernovae missions to falsify the standard model with no spatial curvature. A related issue is a well-known tension between local H_0 measurements and the Hubble constant inferred from the CMB acoustic peaks. One could ask if this discrepancy is artificially tightening the constraints in flat ΛCDM. While it does impact the mean spatial curvature posteriors towards positive values, which also shifts the mean $H(z)$ predictions as seen in Fig. 4, it does not affect the width of the posteriors significantly.

Allowing curvature to be a free parameter broadens the 95% contours on the growth function and the comoving angular diameter distance by a factor of ≈2 (see Fig. 4). Moreover, the posterior of the Hubble parameter becomes monotonic with redshift; i.e., there is no more degeneracy between changes in the H_0 at low redshift and variations in the comoving distance at high redshift. In the curved scenario, the posterior means of all the three functions shown in Fig. 4 shift at the two-sigma level in comparison to the flat ΛCDM case. These variations are mainly induced by the discrepancy between the local H_0 measurements and the angular position of the CMB peaks. Indeed, a positive spatial curvature is correlated with higher H_0 prediction at a fixed angular position of the CMB peaks.

Going from the current JLA data to the simulated WFIRST type IA supernovae tightens posteriors by 40% to 50% in both flat and curved ΛCDM scenarios. The MCMC runs with simulated WFIRST supernovae are somewhat pessimistic because they assume that errors in H_0 will still be at the 2.4% level by the end of the next decade, while Gaia and JWST could potentially bring the

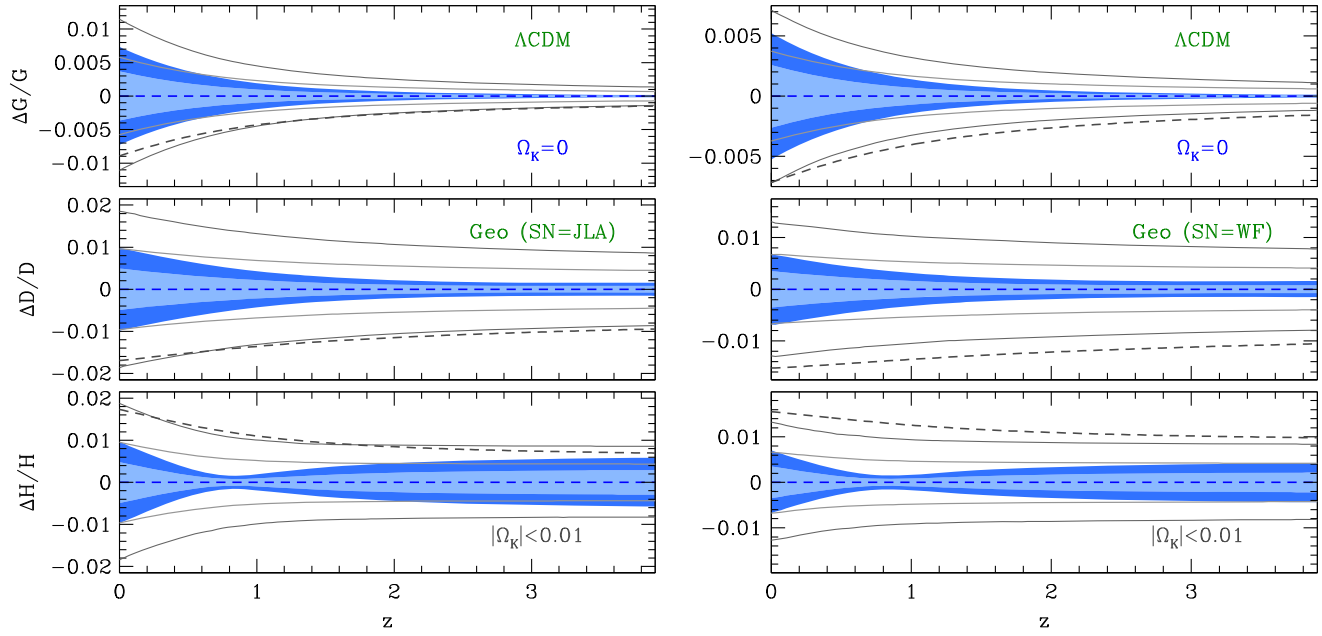

FIG. 4. Constraints on the growth function, the comoving luminosity distance, and the Hubble expansion rate, predicted in the ΛCDM scenario. The blue contours and the grey lines show the 68% (light) and 95% (dark) confidence region assuming no curvature ($\Omega_k = 0$) and the flat prior $|\Omega_k| < 0.01$ (which is noninformative), respectively. In both cases, the confidence levels were centered at zero to highlight the broadening of the posterior. Dashed lines show the fractional difference of the posterior means to flat ΛCDM. The likelihoods adopted in these chains are shown in Table I, with the supernovae given by the JLA compilation on the left panel and the WFIRST simulated data on the right panel. For flat ΛCDM, the remaining freedom on the growth function and the comoving luminosity distance is less than a percent on the entire redshift range, even though the Hubble constant is measured at the 2.4% level. As noted by Ref. [29], flat ΛCDM predictions on the Hubble expansion rate are especially tight around $z \approx 1$, which opens an interesting window of opportunity for model testing by future experiments.

errors down to a subpercent level [43]. Another possibility for measuring H_0 with better precision may come from strong-lensed type IA supernovae. However, refinements in the H_0 precision could also exacerbate the current tension between local measurements and the CMB.

Constraints on the growth function are approximately at the 0.5% level with current data in flat ΛCDM. Marginalization over spatial curvature increases the error on the growth function by a factor of 2, and it also shifts down the growth posterior mean by almost a percent at redshift $z = 0$. The growth rate shows a similar behavior (see Fig. 5). Future updates on the analysis presented in Ref. [53], which translates growth predictions to counts of massive clusters, may prove worthwhile to pursue given that the current H_0 discrepancy pushes the growth function in curved models to values below the flat case. Finally, Fig. 5 shows that ΛCDM has tight predictions on the growth index, which offer an alternative test that can be used to falsify the standard model.

B. Quintessence

Quintessence scenarios offer a wider range of predictions that could still be compatible with data even in the case in which the ΛCDM scenario is falsified by future surveys. From a physical standpoint, scalar fields with dynamics dictated by Lagrangians of the form $\mathcal{L} = X - V$, where X and V are the field's kinetic energy and potential energy, respectively, could drive the accelerated expansion with an equation of state that remains above the phantom barrier of $w = -1$. Quintessence is, therefore, one of the simplest ΛCDM generalizations. In this section, we model quintessence scenarios with the complete set of principal components. To impose the canonical scalar field boundaries $-1 < w(z) < 1$, we adopt the set of conservative priors on the PC amplitudes that are shown in Eqs. (12) and (14), with $w_{\rm min} = -1$ and $w_{\rm max} = 1$.

Quintessence predictions for the growth function are four times broader relative to the ones assuming ΛCDM. Also, there is a 2% shift downwards in the growth's posterior mean, present in runs with either current JLA supernovae or future WFIRST simulated data. The shift downwards in the mean and the broadening of the contour widths show that the growth function in quintessence never exceeds the mean ΛCDM expectation by more than approximately 2% [29]. Consequently, the growth posteriors showed in Fig. 6 provide an exciting possibility of falsifying quintessence and ΛCDM simultaneously. Indeed, modifications of gravity often introduce new degrees of freedom, and they generically enhance the amplitude of linear perturbations well above ΛCDM predictions.

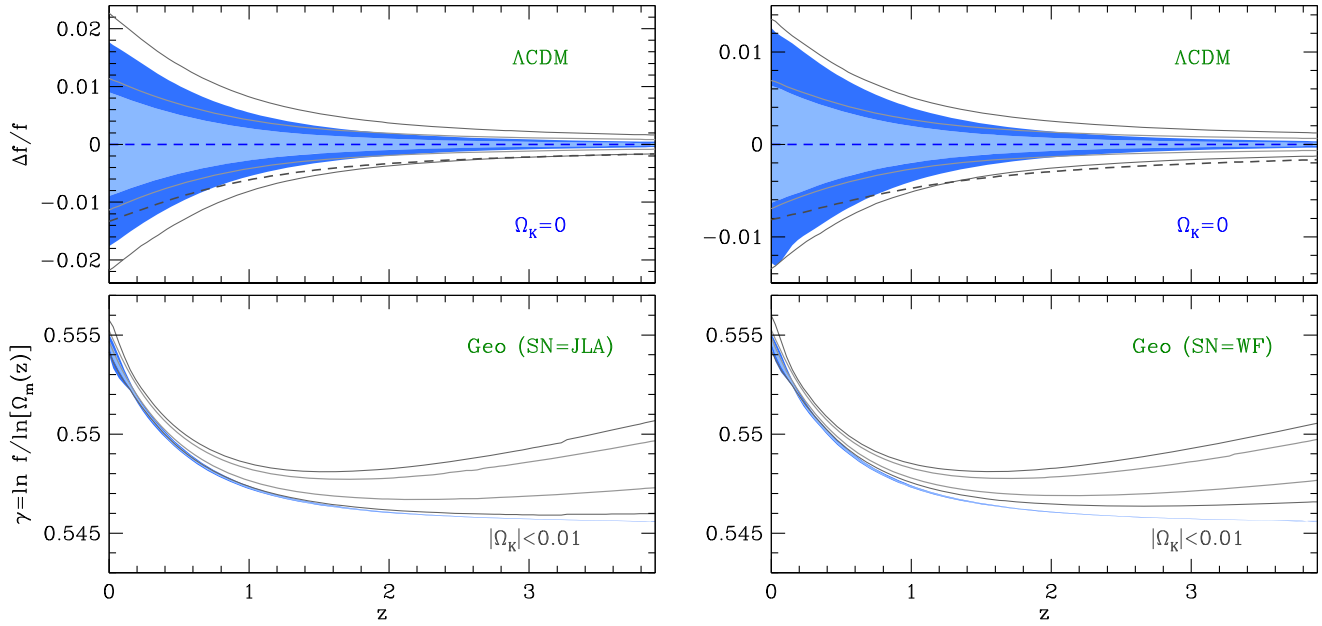

FIG. 5. Constraints on the growth rate and the growth index, predicted by ΛCDM models. The blue contours show the 68% (light) and 95% (dark) confidence region assuming no curvature ($\Omega_k = 0$), while the solid grey lines assume the prior $|\Omega_k| < 0.1$. In both cases, the confidence levels were centered at zero to highlight the broadening of the posterior. Dashed lines show the fractional difference of the posterior means relative to flat ΛCDM. Table I shows the likelihoods adopted in these chains, with the supernovae data given by the JLA compilation (left panel) and the WFIRST simulated data (right panel). Predictions for flat ΛCDM are so tight that the shades are barely visible in the lower panel.

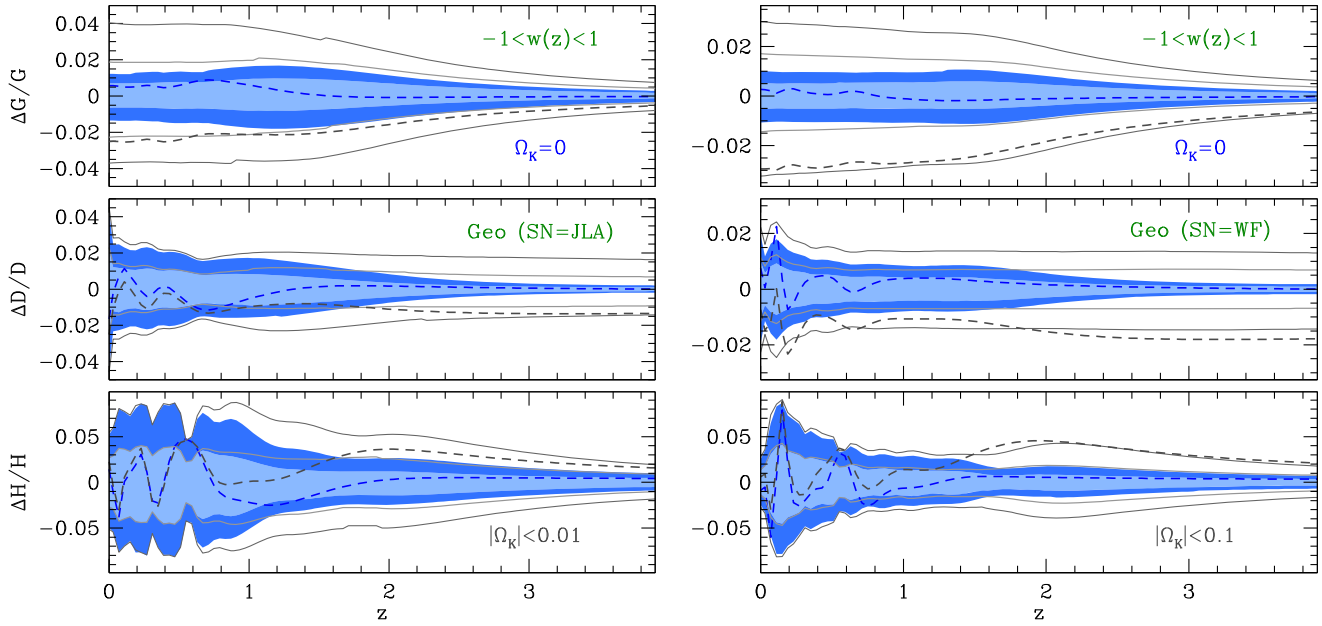

FIG. 6. Similar to Fig. 4, but in the context of quintessence. For future WFIRST data, we relax the spatial curvature prior to $|\Omega_k| < 0.1$. Current observations constrain the Hubble expansion rate better than 10% in flat models, but predictions above $z > 1$ depend considerably on the allowed curvature. The more stringent $|\Omega_k| < 0.01$ prior is necessary to obtain percent-level predictions with current data (see Sec. V for further discussion on this issue). WFIRST, on the other hand, tightens the distance posterior to a few percent even when marginalizing over arbitrary curvature. Finally, the growth function in quintessence never exceeds ΛCDM predictions by more than 2%–3%, and this allows both models to be simultaneously falsified [29].

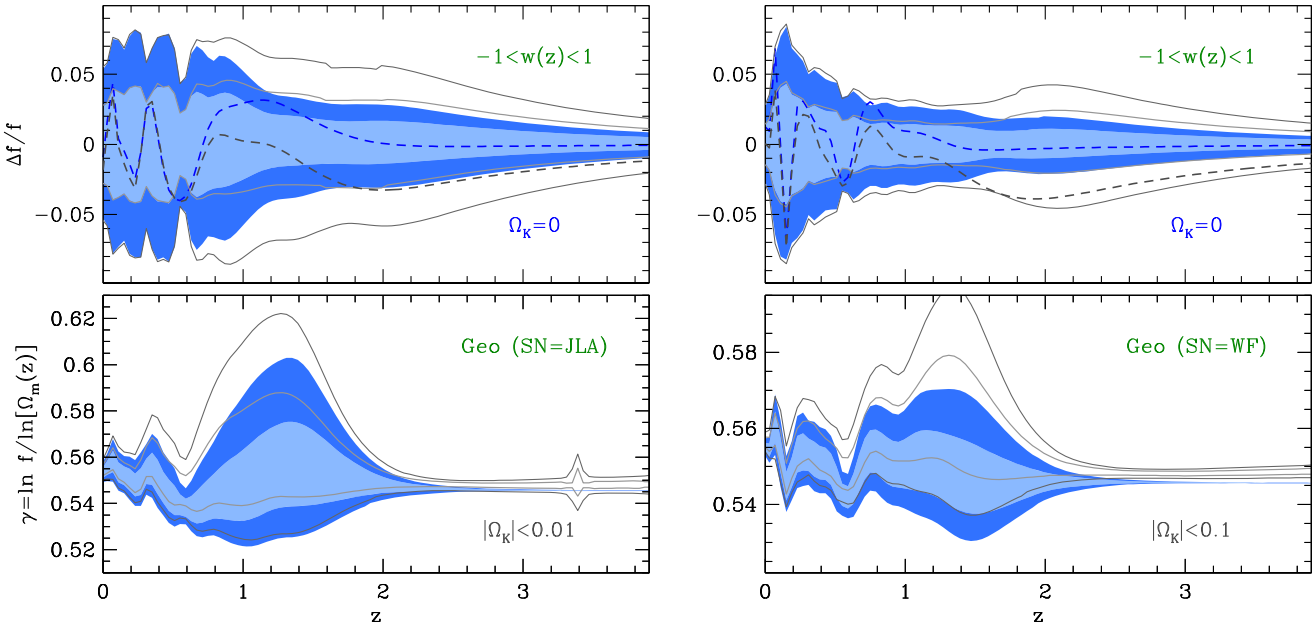

FIG. 7. Similar to Fig. 5, but in the context of quintessence. For future WFIRST data, we relax the spatial curvature prior to $|\Omega_k| < 0.1$. In all models, dark energy is modeled with 20 PCs at $z < z_{\rm max} = 3$ and with $w(z > z_{\rm max}) \equiv w_\infty = -1$.

The comoving luminosity distance posteriors in flat quintessence models are about twice as wide as in ΛCDM. At the same time, the Hubble function is a factor 5 as broad as the standard model at the redshift range $0 < z < 1$. The broadening of the Hubble function is mainly due to highly oscillatory and not-well-constrained modes that are suppressed in the comoving luminosity distance. Indeed, the integration of the Hubble function smooths oscillatory behavior. In flat quintessence, chains with WFIRST type IA supernovae show a 30% improvement in precision in comparison to that obtained with current data. On the other hand, WFIRST constraints show order-unity improvements when spatial curvature is a free parameter. Indeed, present data are not powerful enough to provide percent-level predictions when marginalized over the more extensive range $|\Omega_K| < 0.1$. WFIRST, on the other hand, will be able to constrain the comoving luminosity distance at the 3% level, even when marginalized over arbitrary values of Ω_K. Finally, both flat and curved quintessence scenarios show an order of magnitude broadening in the growth index posterior compared to ΛCDM. The growth rate posterior is also wider, by a factor of 2 approximately, compared to ΛCDM (see Fig. 7).

C. Smooth dark energy

In this subsection, we have adopted the prior $-2.5 < w(z) < 1$ on the dark energy equation of state to reduce the computational requirements of the demanding MCMC likelihood analysis that we present here and in the subsequent sections. To quantify the loss of generality, we simulated WFIRST data and free curvature, where we assume either $-2.5 < w(z) < 1$ or $-5 < w(z) < 1$, and we found no appreciable change. The change in the $w(z)$ prior widens the growth function at redshift $z = 0$ by no more than 15%. Nonetheless, an even ampler range in the equation of state together with the possibility that dark energy could have been relevant at earlier times may degrade growth predictions by a considerable amount. Also, the lack of constraining power in the spatial curvature stretches the posteriors in runs with current data by more than 15%. In any case, falsifying smooth dark energy models with $-2.5 < w(z) < 1$ and no significant amount of early dark energy would already be an enormous step towards motivating more exotic dark energy scenarios.

In comparison to quintessence, Fig. 8 shows that crossing the phantom barrier widens the growth function posterior at $z = 0$ by 40% and the comoving luminosity distance posterior by 30% at $z > 2$, in MCMC runs where we use current data and $|\Omega_K| < 0.01$ prior on the spatial curvature. With WFIRST simulated data and $|\Omega_k| < 0.1$, predictions for the growth function at redshift $z = 0$ are at least 50% larger, while for the comoving luminosity distance they are about 25% broader, relative to the quintessence scenario. Both the growth function and the comoving luminosity distance posterior means are displaced by a few percent in comparison to quintessence predictions. Unlike in quintessence scenarios, the growth function in smooth dark energy models can exceed flat ΛCDM predictions by more than 2%.

The geometric data with simulated WFIRST supernovae will be able to probe the spatial curvature at the percent level. Indeed, WFIRST will be able to constrain the dark energy dynamics so tightly that there will not be enough freedom to compensate the shifts in the comoving distance

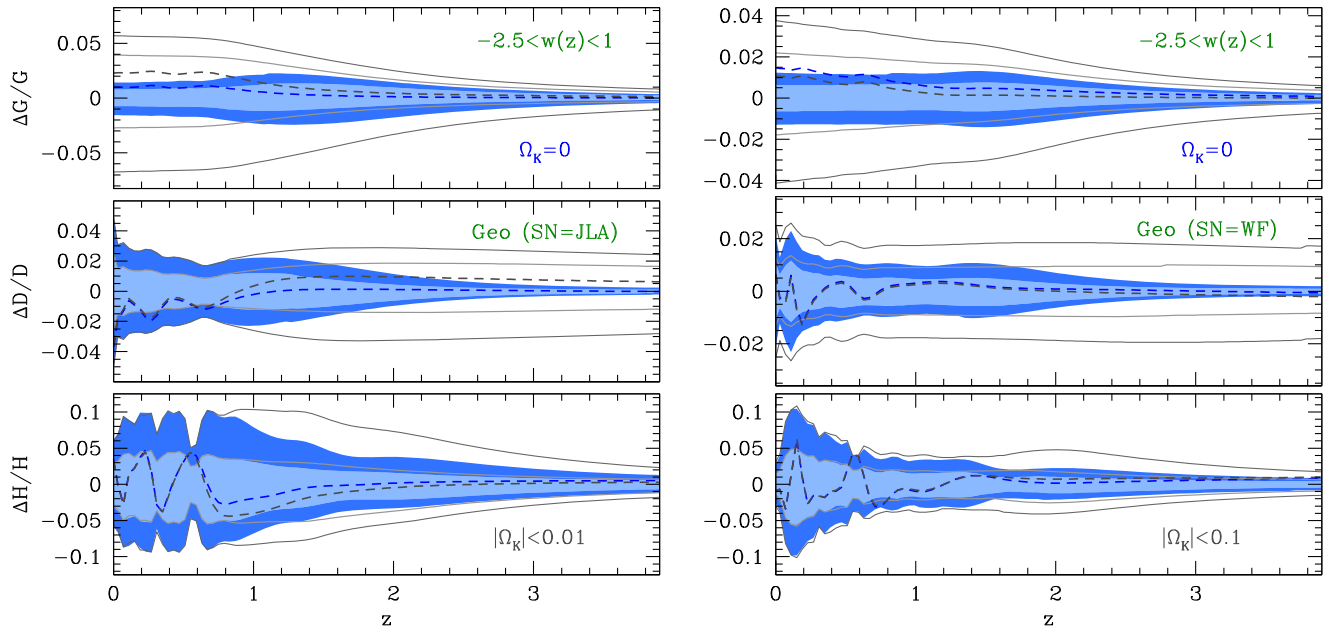

FIG. 8. Similar to Fig. 6, but in the context of smooth dark energy scenarios, where the dark energy equation of state is restricted to the range $-2.5 < w(z) < 1$. The extra freedom provided by the phantom crossing in curved models widens the growth function posterior at redshift zero by approximately 40% with current JLA supernovae and 25% with WFIRST simulated data, in comparison to quintessence models (see Fig. 6). General smooth dark energy scenarios also predict values for the growth function that are substantially higher (5%–7%) than the ΛCDM predictions. Future WFIRST should be able to constrain the comoving distance at the 2% level and the growth function at the 4% level even when marginalizing over arbitrary curvature.

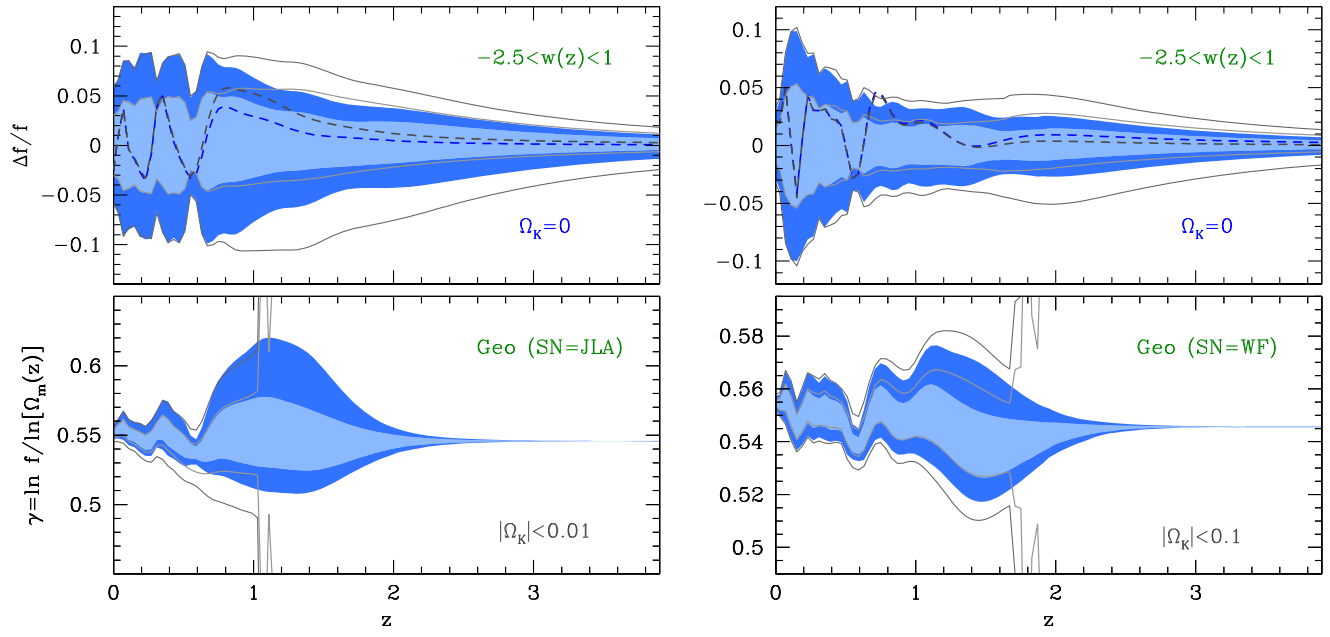

FIG. 9. Similar to Fig. 7, but in the context of smooth dark energy models where the dark energy equation of state is restricted to the range $-2.5 < w(z) < 1$. The extra freedom provided by the phantom crossing in curved scenarios widens the growth rate by approximately 25% above $z = 1$. The posteriors for the growth index $\gamma(z) = \ln f(z)/\ln \Omega_m(z)$ become unstable immediately above redshift $z = 1$. This problem in the growth index happens because $\Omega_m(z)$ can cross the boundary $\Omega_m(z) = 1$ at high redshifts in curved scenarios. The same goes for $f(z)$, but the crossing $f(z) = 1$ happens at slightly different redshifts [29]. This unmatched crossing makes the posteriors either change sign or diverge, and hence the growth index loses its capability to falsify curved smooth dark energy scenarios.

induced by changes in curvature to maintain the distance to the last scattering fixed. With current data, however, constraints on Ω_K are considerably relaxed, which motivates the analysis we present in Sec. V. There, we show how the combination $\sigma_8\Omega_m^{1/2}$ can break the degeneracy between the dark energy equation of state and the spatial curvature. The inclusion of weak lensing, CMB lensing reconstruction, and redshift space distortion data makes an order-unity difference in the dark energy figure of merit after marginalization over spatial curvature.

Finally, Fig. 9 shows that the posteriors for the growth index $\gamma(z) = \ln f(z)/\ln \Omega_m(z)$ become unstable immediately above redshift $z = 1$. Even with the WFIRST simulated supernovae data, the growth index posteriors become ill-behaved above redshift $z \approx 1.5$. This problem in the growth index happens because $\Omega_m(z)$ can cross the boundary $\Omega_m(z) = 1$ at high redshifts, in curved scenarios. The same goes for $f(z)$, but the crossing $f(z) = 1$ happens at slightly different redshifts [29]. This unmatched crossing makes the posteriors either change signs or diverge, and hence, the growth index loses its capability to falsify curved smooth dark energy scenarios. The growth rate, on the other hand, is still well behaved on the entire redshift range, and above $z = 1$, its posteriors are about 25% broader in smooth dark energy scenarios compared to quintessence models. This widening applies to chains with the current JLA data and with the $|\Omega_K| < 0.01$ prior, as well as to chains with the WFIRST simulated data and with $|\Omega_K| < 0.1$.

IV. FIGURE OF MERIT

In this section, we construct a model-independent figure of merit (FoM), making use of the principal components, following closely Ref. [35]. We compute the FoM of the three cosmic acceleration scenarios we have studied so far: ΛCDM, quintessence, and general smooth dark energy scenarios where $-2.5 < w(z) < 1$. PCA-based FoM provides a complementary view to studies that assume particular functional forms for $w(z)$. These studies have the advantage of being more computationally efficient given the low number of parameters involved in parametrizations that are common in the literature. FoMs based on particular functional forms for $w(z)$ also have a straightforward interpretation regarding signal-to-noise ratio. However, FoMs based on particular forms of $w(z)$ may underestimate or overestimate the constraining power of a given experiment, given that there are multiple compelling generalizations of ΛCDM, without a clear hierarchy between them in terms of theoretical plausibility.[4] They provide, therefore, an incomplete picture about the future capabilities of WFIRST in constraining dark energy models that predict more elaborate forms of $w(z)$. This incompleteness depends on how typical values for the amplitudes α_i compare with the 68% and 95% observational confidence levels on α_i, when the fiducial model is projected on the PCA basis. This is defined as the signal-to-noise ratio [see Eq. (3) in Ref. [55]].

For example, Ref. [35] confirms that models in which the dark energy dynamics is dictated by a canonical field, ϕ, that rolls on a potential of the form $V(\phi) = V_0 + m^2\phi^2/2$ have small projected volumes in the subspace spanned by all except for the two most constraining principal components.[5] Indeed, Fig. 5 of Ref. [35] explicitly shows, for a particular choice of parameters, that only the first and second principal components have amplitudes that are comparable to their respective posterior uncertainties. While $V(\phi) = V_0 + m^2\phi^2/2$ is a perfectly reasonable potential, there is not enough theoretical guidance from a more fundamental particle description of the dark energy component to prevent us from constructing more convoluted potentials that result in a $w(z)$ that needs to be described with more principal components.

These nuances in interpreting the FoMs based on particular parametrizations, when there are multiple compelling dark energy models, can affect the design choices for future experiments in ways that could potentially reduce the possibility of discovering ground-breaking results. For example, the FoM based on $w(z) =$ constant models predicts that the best supernovae strategies are the ones that focus their statistical power at the low-redshift range $z < 1$. A similar conclusion can be derived from simple models where $w(z)$ is well described, in terms of signal to noise, by the first few PCA components of the Imaging-Allz strategy. However, observational strategies that focus on low-z supernova could lose the possibility of investigating models that predict $w(z)$ with large projected volume on the subspace spanned by higher principal components of the Imaging-Allz strategy (which would boost the signal-to-noise ratio of these components).

Following Ref. [35], we define the figure of merit, given the covariance $\mathbf{C}_n$ between the principal components $e_i(z)$ with $i = 1, \ldots, n$, as

$$\mathrm{FoM}_n^{\mathrm{PC}} = \left(\frac{\det \mathbf{C}_n}{\det \mathbf{C}_n^{\mathrm{prior}}}\right)^{-1/2}. \tag{15}$$

Here, $\mathbf{C}_n^{\mathrm{prior}}$ is the covariance of the prior, which we estimate based on MCMC chains that only take into account the prior constraints on $w(z)$ in Eqs. (12) and (14).[6] While not all parametrizations with n parameters necessarily show the

[4] Indeed, nonparametric methods such as PCAs are well suited to observables that cannot be robustly modeled from first-principle calculations. They have been used, for example, to describe inflation and the epoch of reionization [51,54].

[5] The PCs of Ref. [35] were constructed to mimic the discontinued SNAP experiment [56].

[6] This FoM definition depends on the prior volume, which might seem contrived, but by doing so we eliminate information gain that comes exclusively from the prior [35]. This can also be achieved by only considering the FoM ratio between two experiments [57].

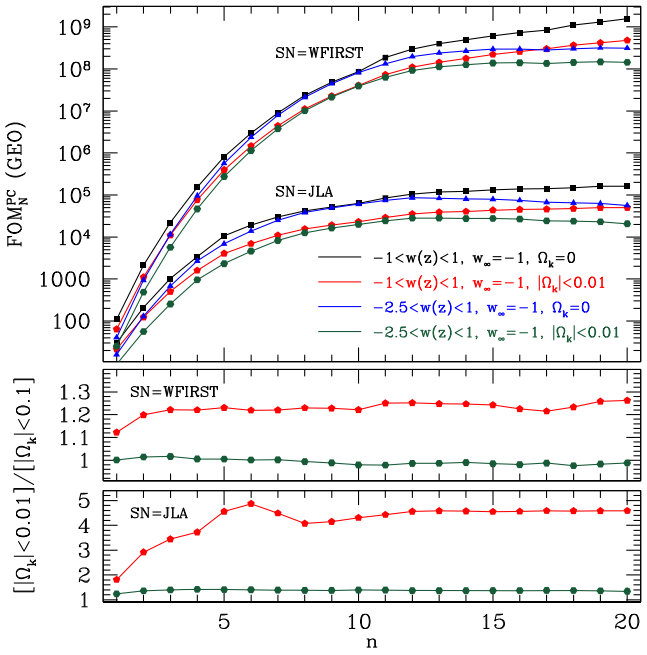

FIG. 10. Figure of merit of the PC amplitudes when the smooth dark energy scenario is probed with Planck geometric data, BAO, local H_0, and JLA/WFIRST type IA supernovae measurements, as a function of the number of principal components. Current data can measure the first five principal components approximately. WFIRST will be able to measure these first five components significantly better and, in total, it will be able to constrain twice the number of modes. Finally, spatial curvature impacts the FoM derived from current data at order unity, while only at a few tens of percent with WFIRST simulated data.

improvement given by FoM_n, this quantity represents an approximate upper limit of what is achievable with a given experiment. The quantity $\mathrm{FoM}_n^{\mathrm{PC}}$ is only an approximate upper limit because our PCs were developed with the Fisher matrix and not with the actual likelihood of the experiment. The interpretation of $\mathrm{FoM}_n^{\mathrm{PC}}$ with $n \ll 20$ as an upper limit for the background data with the current JLA data has an additional caveat, given that we use the same PC basis for both JLA and WFIRST experiments. However, the asymptotic value, $\mathrm{FoM}_{n\approx 20}^{\mathrm{PC}}$, can robustly be interpreted as an upper limit to both JLA and WFIRST because these 20 PCs span a complete basis to both experiments.

Figure 10 compares the PCA-based figure of merit between the analysis with the JLA compilation and the WFIRST simulated data. Both cases include BAO, geometric CMB, and local H_0 measurements. Current data can place a good measurement on approximately the first five principal components. The FoM for these modes is $\mathrm{FoM}_{n=5}^{\mathrm{PC}}(\mathrm{SN}=\mathrm{JLA}) \approx 10^4$, while $\mathrm{FoM}_{n=2}^{\mathrm{PC}}(\mathrm{SN}=\mathrm{JLA}) \approx 10^2$ and therefore two-parameter descriptions of $w(z)$, such as the commonly adopted $w_0 - w_a$, do not exhaust the information that can be extracted from current data. Future WFIRST data will be able to better constrain the first five principal components $[\mathrm{FoM}_{n=5}^{\mathrm{PC}}(\mathrm{SN}=\mathrm{WF}) \approx 10^6]$, and it will also probe twice the number of principal components in comparison to JLA type IA supernovae. Indeed, WFIRST will have a wider redshift range sensitive to modes that affect $w(z)$ only at high redshift. The asymptotic FoM ratio between these two data sets is of order 10^4, while this ratio is on the order of 10 for the $w_0 - w_a$ parametrization.

In the $w_0 - w_a$ functional form, the high and low redshift are entangled, and therefore many of the modes that only WFIRST can measure well are not allowed by prior or are severely restricted by the low-redshift supernovae data. Thus, simple two-parameter functional forms of $w(z)$ offer an incomplete picture of the modes that can be measured with current and future data. Including extra parameters in popular parametrizations, however, does not guarantee that the signal-to-noise ratio of higher order PCAs will be greater than unity and, therefore, the approximate upper limit in FoM_n may be quite difficult to achieve. This limitation indeed seems to hold, as it has been shown that the signal-to-noise ratio in $e_{n\gg 3}(z)$ PCAs, constructed to be representative of experiments that resemble WFIRST, is small in commonly adopted quintessence models [55,58,59]. Without selection criteria derived from a more fundamental description of dark energy, our results merely indicate that, in principle, it is possible to construct smooth dark energy models that are elaborate enough so that improvements in $\mathrm{FoM}_n^{\mathrm{PC}}$ with $n \gg 3$ represent a gain of information provided by next generation of experiments.[7]

In quintessence scenarios, priors in the allowed curvature range make a significant impact on the figure of merit (as shown in Fig. 11). Indeed, Fig. 12 shows that curvature cannot be constrained at the few-percent level with current data if we assume quintessence, and the uniform prior $|\Omega_K| < 0.1$ decreases the FoM by approximately an order of magnitude in comparison to the flat $\Omega_K = 0$ case. In general, in smooth dark energy models that respect the boundary $-2.5 < w(z) < 1$, the curvature posterior disfavors large positive values. However, the chosen uniform priors in the amplitude of the principal components is not mapped into flat spatial curvature posteriors, and in fact the priors provide more weight to models that do cross the phantom barrier (see Fig. 12 of [29]).

The inability of current geometric data to constrain spatial curvature at the percent level when Ω_K is marginalized over quintessence and general dark energy models provides an excellent opportunity for observables that directly measure the growth of structure to make a significant impact on the figure of merit. Growth information could also mitigate, in the context of ΛCDM, the

[7]The PCA merely shows the modes that can be constrained by the data (and how well they can be constrained). Interpretation of the subspace spanned by these PCs depends on theoretical analysis that is out of the scope of statistical tools that rely only on the data.

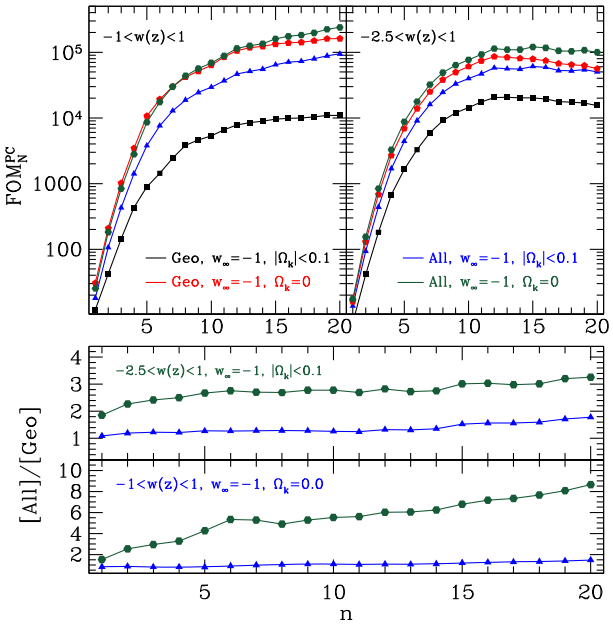

FIG. 11. The figure of merit of the PC amplitudes when quintessence (top left panel) and smooth dark energy (top right panel) are probed with either the Geometric or the All data sets. For quintessence, direct measurements of the growth of structure make an order of magnitude change on the FoM values, as it decreases the posterior probabilities of large and positive Ω_K. For general smooth dark energy, the difference in the FoM is not as dramatic when growth information is combined, but given that flat priors to the PC amplitudes translate into a preference for negative curvature, part of this reduction in the FoM ratio might be prior induced, which itself reduces the posterior for large and positive Ω_K.

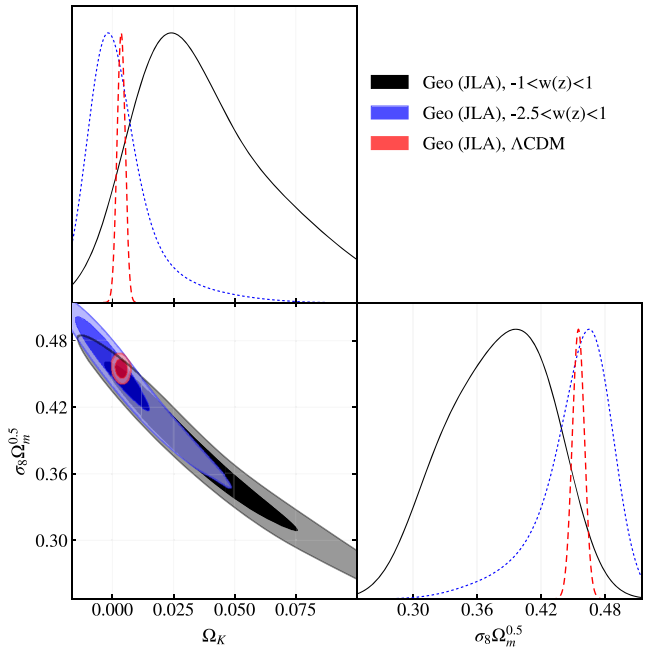

FIG. 12. Spatial curvature posterior and its strong correlation with the combination $\sigma_8\Omega_m^{1/2}$. The inability of current geometric data to constrain spatial curvature at the percent level in both quintessence and general dark energy models provides an excellent opportunity for observables that directly measure the growth of structures to make a significant impact on the dark energy figure of merit. Finally, given that flat priors (that can also cross the phantom barrier) on the PC amplitudes translate into a preference for negative curvature, the reduction of the posterior probability for large and positive Ω_k in general dark energy models might be partially prior induced (see Fig. 12 of [29]).

impact of the discrepancy between the CMB and local H_0 measurements, which shifts the spatial curvature posterior towards positive values. The combination of the full CMB temperature and polarization power spectra, CMB lensing reconstruction, redshift space distortions, and weak lensing measurements should indeed constrain curvature tightly given that we see a strong correlation between Ω_K and the predicted $\sigma_8\Omega_m^{1/2}$ in all our Geo chains with current JLA supernovae (see Fig. 12). Indeed, the combination $\sigma_8\Omega_m^{1/2}$ corresponds to the direction in parameter space that is best measured by weak lensing.

With the simulated WFIRST supernovae data, Ω_K is constrained at the percent level in both quintessence and smooth dark energy scenarios (see Fig. 13), and this provides an interesting challenge for the future WFIRST weak lensing survey. Current weak lensing surveys, including the recently published Year One DES measurements, are discrepant with CMB inferences on $\sigma_8\Omega_m^{1/2}$ at the two-sigma level. Also note that our results do not imply that every single quintessence and smooth dark energy model will have Ω_K uncertainties larger than a percent. What we show is what happens when we are agnostic concerning the feasibility of arbitrary complicated smooth dark energy scenarios.

Finally, the model-independent FoM$_n^{\rm PC}$ can be converted into model-based figure of merit evaluations with the use of a fast approximate likelihood that dispenses with the use of expensive additional MCMC calculations, as well as the use of sophisticated numerical packages such as CosmoMC. Given the discrete set of parameter values $\alpha_i = \{\alpha_1, \ldots, \alpha_{20}\}$ and multiplicities w_i provided by our MCMC chains, we define a kernel density estimation likelihood of the form [51]

$$\mathcal{L}_{\rm PC}(\text{data}|\boldsymbol{\alpha}) = \sum_{i=1}^{N} w_i K_f(\boldsymbol{\alpha} - \boldsymbol{\alpha}_i). \tag{16}$$

Here N is the number of elements in the chain, K_f is a smoothing kernel that we assume to be a multivariate Gaussian with zero mean and covariance $f\mathbf{C}_{n=20}$ (f is a smoothing factor), and α is the set of values generated by the model to be constrained. Such a technique has been applied with remarkable success in the context of model-independent studies on the epoch of reionization [51,60]. The posterior for any physically motivated parametrization with M parameters $\boldsymbol{\beta} = \{\beta_1, \ldots, \beta_M\}$ is

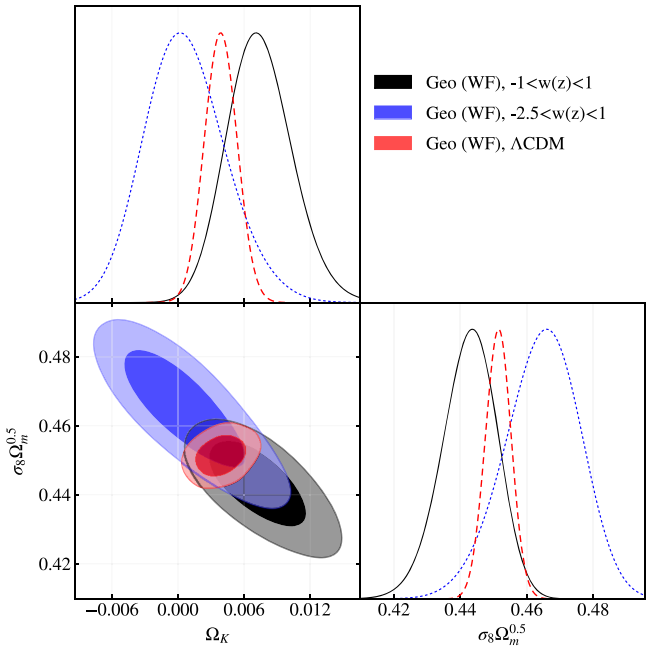

FIG. 13. Spatial curvature posterior and its correlation with the combination $\sigma_8\Omega_m^{1/2}$. Further improvements in BAO measurements from the future DESI survey as well as advances in local H_0 measurements may bring Ω_K constraints to the subpercent level without growth information.

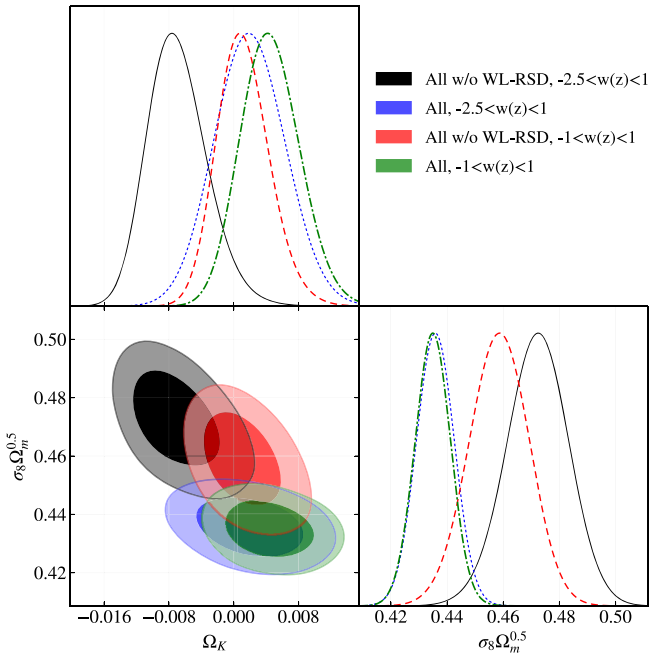

FIG. 14. Posterior of curvature and its correlation with $\sigma_8\Omega_m^{1/2}$. It is clear that the tension between CMB measurements by the Planck satellite and low-redshift structure probes shifts Ω_K at the two-sigma level. In particular, no claims that curvature is measured at the subpercent level, when marginalized over smooth dark energy models, can be made without solving this tension.

$$P(\boldsymbol{\beta}|\text{data}) \propto \mathcal{L}_{\text{PC}}(\text{data}|\boldsymbol{\alpha}(\boldsymbol{\beta}))P(\boldsymbol{\beta}). \tag{17}$$

We then can define model-based FoM as $\text{FoM}_M^{\text{Model}} = (\det \mathbf{C}(\beta_1, \ldots, \beta_M))^{-1/2}$. Such a posterior also allows the signal-to-noise ratio of each principal component to be fully sampled for arbitrary models. We intend to fully explore this technique in a future work to be accomplished in collaboration with the WFIRST supernova science investigation teams.

V. IMPROVING SPATIAL CURVATURE CONSTRAINTS WITH GROWTH INFORMATION

In this section, we will use the PCA basis of $w(z)$ to quantify the effects of marginalizing the spatial curvature posterior over different classes of dark energy models. We will restrict our analysis to current data, including information from the growth of structure. In a follow-up study, we will investigate the correlations between dark energy parameters and spatial curvature for the future WFIRST mission, including the WFIRST weak lensing survey. We will also quantify the correlations between the sum of neutrino mass constraints and dark energy scenarios.

In the context of the ΛCDM model, the combination of the full CMB temperature and polarization spectra from the Planck satellite with BAO measurements constrains the spatial curvature to the subpercent level $|\Omega_K| < 0.005$ [61]. Figure 12 shows that even data sets that only measure the background expansion of the Universe can, all together, probe the curvature to within a percent. However, the discrepancy between the CMB and local H_0 measurements shifts the central value of the spatial curvature posterior towards positive values. For quintessence models, Fig. 12 shows that geometric data cannot constrain spatial curvature even at the 10% level. The situation changes slightly for general smooth dark energy models for which $-2.5 < w(z) < 1$. However, this shift towards negative spatial curvature is in part due to our choice of priors, given that uniform priors in the PCA amplitudes α_i do not translate into a flat posterior in the spatial curvature [29].

The remaining freedom in the spatial curvature posterior can be significantly reduced by constraining the product $\sigma_8\Omega_m^{1/2}$, which is the parameter combination that weak lensing measures best. CMB temperature and polarization power spectra can also constrain the curvature up to the percent level due to the gravitational lensing effect that smooths the acoustic peaks. Indeed, Fig. 14 shows that the posterior width of Ω_K is reduced by more than a factor of 10 in the context of quintessence models when the Gaussian CMB likelihood is replaced by the full CMB temperature and polarization spectra. Even for arbitrary smooth dark energy models, with $-2.5 < w(z) < 1$, the spatial curvature can be constrained better than 1.5% with the full CMB power spectrum.

In both quintessence and smooth dark energy paradigms, the effect of marginalizing the dark energy principal

components in addition to spatial curvature is to reduce the FoM by a factor of a few. More specifically, the FoM is reduced by ≈10 in quintessence scenarios, primarily because of the non-negligible posterior probability for large and positive Ω_K, and by ≈5 in smooth dark energy scenarios, as shown in Fig. 11. This level of improvement is significantly higher than in ΛCDM. Indeed, the spatial curvature is constrained by both geometry and growth information in the standard model, given that there is not enough freedom in the dark energy sector to compensate for changes in the background expansion induced by large values of Ω_K to maintain the comoving distance to the surface of the last scattering unchanged.

The addition of low-redshift probes that measure growth, such as weak-lensing and redshift space distortion, shifts the curvature posterior by an amount comparable to the 95% confidence regions, in comparison to the All w/o WL-RSD MCMC chains (see Fig. 14). Indeed, the combination $\sigma_8\Omega_m^{1/2}$ is well constrained by weak lensing, and there is a two-sigma tension between weak lensing and the CMB, which reflects into doubling the uncertainties in constraining spatial curvature marginalized over smooth dark energy scenarios.

VI. DISCUSSION

In this paper, we provide a comprehensive investigation on how current data that probe the background expansion constrain the theoretical predictions of three broad classes of dark energy: ΛCDM, quintessence, and smooth dark energy models that respect the prior $-2.5 < w(z) < 1$. These three paradigms share the property that dark energy influences the growth of structure by modifying the background expansion.

Within this framework, we show that the current background expansion predicts the linear growth of structure at the percent level. For general smooth models, such predictions are at the 10% level when marginalizing over the informative prior $-0.01 < \Omega_k < 0.01$. Flat models always predict growth at the few-percent level, which provides an exciting opportunity for current and future surveys to falsify the flat, smooth dark energy scenario with weak lensing and redshift-space distortion measurements.

WFIRST supernovae data will be able to improve growth predictions in curved models significantly. In particular, the two-sigma posterior for $G(z)$ is at the 8% level even when marginalizing over the noninformative prior $-0.1 < \Omega_k < 0.1$. Our analysis is conservative because it neglects upcoming BAO improvements from the future DESI survey as well as advancements in measuring the local H_0.

In the near future, the degeneracy between spatial curvature and $w(z)$ could be mitigated with measurements of the combination $\sigma_8\Omega_m^{1/2}$. Indeed, this is the direction in parameter space that weak lensing measurements restrict the most. In fact, the inclusion of CFHTLens and DR12 RSD measurements reduces the figure of merit of the PCA amplitudes by order unity. We also point out that inconsistencies between low-redshift measurements and CMB predictions for $\sigma_8\Omega_m^{1/2}$ translate into uncertainties in constraining Ω_k marginalized over the PCA amplitudes.

Finally, we evaluate a PCA-based figure of merit, which reveals that a two-parameter description of $w(z)$ may not provide the complete picture of advancements in constraining power between WFIRST and JLA supernovae surveys. In particular, specific $w(z)$ functional forms may bias the determination of the optimal redshift range for the WFIRST supernovae survey. While a shallow survey can provide better statistics, a more extensive range may probe a broader range of models.

ACKNOWLEDGMENTS

We thank R. Hounsell, D. Scolnic, R. J. Foley, and R. Kessler for helpful discussions and for providing us state-of-the-art WFIRST simulated supernova. We also thank R. Kessler and W. Hu for providing us extensive computational resources granted by the University of Chicago Research Computing Center. We thank Eric Linder for valuable discussions about the interpretation of the PCA-based figure of merit. V. M. thanks the hospitality of the Sitka Sound Science Center during the intermediate stages of this work. V. M. was supported in part by the Charles E. Kaufman Foundation, a supporting organization of the Pittsburgh Foundation.

[1] A. G. Riess *et al.* (Supernova Search Team), Astron. J. **116**, 1009 (1998).
[2] S. Perlmutter *et al.* (Supernova Cosmology Project), Astrophys. J. **517**, 565 (1999).
[3] A. G. Riess *et al.*, Astrophys. J. **659**, 98 (2007).
[4] M. Betoule *et al.* (SDSS Collaboration), Astron. Astrophys. **568**, A22 (2014).
[5] R. Hounsell, D. Scolnic, R. J. Foley, R. Kessler, V. Miranda, A. Avelino, R. C. Bohlin, A. V. Filippenko, J. Frieman, S. W. Jha, P. L. Kelly, R. P. Kirshner, K. Mandel, A. Rest, A. G. Riess, S. A. Rodney, and L. Strolger, arXiv:1702.01747.
[6] D. J. Eisenstein *et al.* (SDSS Collaboration), Astrophys. J. **633**, 560 (2005).

[7] P. A. Abell *et al.* (LSST Science, LSST Project), arXiv:0912.0201.
[8] L. Amendola *et al.*, Living Rev. Relativity **21**, 2 (2018).
[9] P. A. R. Ade *et al.* (Planck Collaboration), Astron. Astrophys. **594**, A14 (2016).
[10] P. Ade *et al.* (Planck Collaboration), Astron. Astrophys. **594**, A15 (2016).
[11] N. Benitez *et al.* (J-PAS Collaboration), arXiv:1403.5237.
[12] T. Erben *et al.*, Mon. Not. R. Astron. Soc. **433**, 2545 (2013).
[13] J. T. A. de Jong, G. A. Verdoes Kleijn, K. H. Kuijken, and E. A. Valentijn, Exp. Astron. **35**, 25 (2013).
[14] A. G. Riess *et al.*, Astrophys. J. **853**, 126 (2018).
[15] T. Abbott *et al.* (DES Collaboration), arXiv:astro-ph/0510346.
[16] H. Aihara *et al.*, Publ. Astron. Soc. Jpn. **70**, 4 (2018).
[17] D. Huterer and A. Cooray, Phys. Rev. D **71**, 023506 (2005).
[18] Y. Wang and M. Tegmark, Phys. Rev. D **71**, 103513 (2005).
[19] C. Zunckel and R. Trotta, Mon. Not. R. Astron. Soc. **380**, 865 (2007).
[20] S. Sullivan, A. Cooray, and D. E. Holz, J. Cosmol. Astropart. Phys. 09 (2007) 004.
[21] G.-B. Zhao, D. Huterer, and X. Zhang, Phys. Rev. D **77**, 121302 (2008).
[22] G.-B. Zhao and X.-m. Zhang, Phys. Rev. D **81**, 043518 (2010).
[23] P. Serra, A. Cooray, D. E. Holz, A. Melchiorri, S. Pandolfi, and D. Sarkar, Phys. Rev. D **80**, 121302 (2009).
[24] J. Kujat, A. M. Linn, R. J. Scherrer, and D. H. Weinberg, Astrophys. J. **572**, 1 (2002).
[25] S. Chongchitnan and G. Efstathiou, Phys. Rev. D **76**, 043508 (2007).
[26] D. Huterer and H. V. Peiris, Phys. Rev. D **75**, 083503 (2007).
[27] H. Zhan, L. Knox, and J. A. Tyson, Astrophys. J. **690**, 923 (2009).
[28] A. Aghamousa *et al.* (DESI Collaboration), arXiv:1611.00036.
[29] M. J. Mortonson, W. Hu, and D. Huterer, Phys. Rev. D **79**, 023004 (2009).
[30] M. J. Mortonson, W. Hu, and D. Huterer, Phys. Rev. D **81**, 063007 (2010).
[31] R. A. Vanderveld, M. J. Mortonson, W. Hu, and T. Eifler, Phys. Rev. D **85**, 103518 (2012).
[32] A. Cooray, D. Huterer, and D. Baumann, Phys. Rev. D **69**, 027301 (2004).
[33] E. J. Ruiz and D. Huterer, Phys. Rev. D **91**, 063009 (2015).
[34] E. J. Ruiz, D. L. Shafer, D. Huterer, and A. Conley, Phys. Rev. D **86**, 103004 (2012).
[35] M. J. Mortonson, D. Huterer, and W. Hu, Phys. Rev. D **82**, 063004 (2010).
[36] A. Lewis, Phys. Rev. D **87**, 103529 (2013).
[37] A. Lewis and S. Bridle, Phys. Rev. D **66**, 103511 (2002).
[38] A. Lewis, A. Challinor, and A. Lasenby, Astrophys. J. **538**, 473 (2000).
[39] C. Howlett, A. Lewis, A. Hall, and A. Challinor, J. Cosmol. Astropart. Phys. 04 (2012) 027.
[40] N. Aghanim *et al.* (Planck Collaboration), Astron. Astrophys. **594**, A11 (2016).
[41] H. Gil-Marín, W. J. Percival, A. J. Cuesta, J. R. Brownstein, C.-H. Chuang, S. Ho, F.-S. Kitaura, C. Maraston, F. Prada, S. Rodríguez-Torres, A. J. Ross, D. J. Schlegel, D. P. Schneider, D. Thomas, J. L. Tinker, R. Tojeiro, M. Vargas Magaña, and G.-B. Zhao, Mon. Not. R. Astron. Soc. **460**, 4210 (2016).
[42] C. Blake, E. Kazin, F. Beutler, T. Davis, D. Parkinson *et al.*, Mon. Not. R. Astron. Soc. **418**, 1707 (2011).
[43] A. G. Riess *et al.*, Astrophys. J. **826**, 56 (2016).
[44] A. G. Riess, L. Macri, S. Casertano, M. Sosey, H. Lampeitl, H. C. Ferguson, A. V. Filippenko, S. W. Jha, W. Li, R. Chornock, and D. Sarkar, Astrophys. J. **699**, 539 (2009).
[45] M. Foley, R. Foley, D. Scolnic, A. Rest, A. G. Riess, S. W. Jha, R. Kirshner, O. Dosovitz Fox, Y.-C. Pan, and S. Smartt, in *American Astronomical Society Meeting Abstracts*, American Astronomical Society Meeting Abstracts, Vol. 229 (2017) p. 341.12.
[46] C. Heymans *et al.*, Mon. Not. R. Astron. Soc. **432**, 2433 (2013).
[47] R. Takahashi, M. Sato, T. Nishimichi, A. Taruya, and M. Oguri, Astrophys. J. **761**, 152 (2012).
[48] L. Casarini, S. A. Bonometto, E. Tessarotto, and P. S. Corasaniti, J. Cosmol. Astropart. Phys. 08 (2016) 008.
[49] L. Casarini, A. V. Maccio', and S. A. Bonometto, J. Cosmol. Astropart. Phys. 03 (2009) 014.
[50] G. Efstathiou and J. R. Bond, Mon. Not. R. Astron. Soc. **304**, 75 (1999).
[51] C. H. Heinrich, V. Miranda, and W. Hu, Phys. Rev. D **95**, 023513 (2017).
[52] E. V. Linder, Phys. Rev. D **72**, 043529 (2005).
[53] M. J. Mortonson, W. Hu, and D. Huterer, Phys. Rev. D **83**, 023015 (2011).
[54] C. Dvorkin and W. Hu, Phys. Rev. D **82**, 043513 (2010).
[55] R. de Putter and E. V. Linder, arXiv:0812.1794.
[56] G. Aldering *et al.* (SNAP Collaboration), arXiv:astro-ph/0405232.
[57] A. Albrecht, L. Amendola, G. Bernstein, D. Clowe, D. Eisenstein, L. Guzzo, C. Hirata, D. Huterer, R. Kirshner, E. Kolb, and R. Nichol, arXiv:0901.0721.
[58] M. Barnard, A. Abrahamse, A. Albrecht, B. Bozek, and M. Yashar, Phys. Rev. D **78**, 043528 (2008).
[59] E. V. Linder and D. Huterer, Phys. Rev. D **72**, 043509 (2005).
[60] V. Miranda, A. Lidz, C. H. Heinrich, and W. Hu, Mon. Not. R. Astron. Soc. **467**, 4050 (2017).
[61] P. A. R. Ade *et al.* (Planck Collaboration), Astron. Astrophys. **594**, A13 (2016).